Radiotherapy and Oncology 222 (2026) 111674

Contents lists available at ScienceDirect

Radiotherapy and Oncology

journal homepage: www.thegreenjournal.com

Original Article

Early ADC changes in risk-model-defined brain regions precede contrast-enhancing lesions after proton therapy for low-grade glioma

Habiba Sallem [a,b,*], Semi Harrabi [a,b], Michael O. Breckwoldt [c], Klaus Herfarth [a,b], Jürgen Debus [a,b,d], Julia Bauer [a,b,e]

[a] Department of Radiation Oncology and Heidelberg Ion Beam Therapy Center, Heidelberg University Hospital, Heidelberg, Germany
[b] Heidelberg Institute for Radiation Oncology (HIRO), National Center for Radiation Research in Oncology (NCRO), Heidelberg, Germany
[c] Department of Neuroradiology, Heidelberg University Hospital, Heidelberg, Germany
[d] Clinical Cooperation Unit Radiation Oncology, German Cancer Research Center (DKFZ), Heidelberg, Germany
[e] Department of Radiation Oncology, Charité - Universitätsmedizin Berlin, Corporate Member of Freie Universität Berlin and Humboldt-Universität zu Berlin, Berlin, Germany

ARTICLE INFO

Keywords:
Low-grade glioma
Proton therapy
diffusion MRI
ADC
Radiation-induced brain injuries

ABSTRACT

Background: Contrast-enhancing brain lesions (CEBLs) are a challenging late effect of proton therapy (PT) in low-grade glioma (LGG), typically detected after blood–brain barrier disruption. Diffusion-weighted imaging (DWI) and derived apparent diffusion coefficient (ADC) metrics can reveal early microstructural alterations preceding this disruption. Their diagnostic value can be enhanced by combining it with voxel-wise risk-modelling, such as the Probability of Lesion Origin (POLO) model, which maps spatial susceptibility to radiation-induced damage. This pilot study investigates the feasibility of combining longitudinal DWI with POLO-based risk stratification to characterize regional tissue response trajectories after PT in patients with and without CEBL.

Methods: Twenty LGG-patients treated with PT were retrospectively analyzed: ten developed CEBLs ($CEBL^{+}$) and ten remained lesion-free ($CEBL^{-}$). Longitudinal ADC-volume-histogram metrics ($ADC_{20\%}$, ADC_{mean}, ADC_{median}) were extracted from POLO-defined high-risk (HR) and low-risk (LR) volumes. Temporal evolution was quantified using coefficients of variation and slopes.

Results: $CEBL^{+}$ patients exhibited higher ADC values, greater temporal variability, and steeper increases over time, especially within HR regions. For $ADC_{20\%}$, HR values exceeded LR in $CEBL^{+}$, while no HR–LR difference was observed in $CEBL^{-}$. The HR–LR $ADC_{20\%}$ difference distinguished $CEBL^{+}$ from $CEBL^{-}$ patients as early as six months post-treatment, yielding AUCs of 0.70–0.79 across quarterly timepoints.

Conclusions: Risk-model-informed interpretation of DWI, considering localized information on anticipated biological damage, demonstrates the potential for quantitative assessment of post-treatment tissue dynamics. Early HR–LR ADC divergence, particularly in $ADC_{20\%}$, may serve as an imaging biomarker for monitoring radiation-induced tissue changes after PT, supporting post-treatment imaging surveillance.

Introduction

Radiation-induced brain injuries are a recognized late complication of proton therapy[1] (PT), particularly in patients with low-grade glioma (LGG). Among these effects, contrast-enhancing brain lesions (CEBLs) represent a clinically challenging manifestation, typically emerging months to years after treatment and affecting approximately 20 % of patients[2]. Depending on their extent and location, CEBLs can range from incidental radiological findings to lesions associated with significant neurological symptoms[3], with the underlying pathophysiology involving vascular damage, demyelination, and white matter injury, ultimately leading to blood–brain barrier disruption [2,4–6]. Conventional contrast-enhanced MRI identifies lesions only after blood–brain barrier disruption has occurred[7], and no validated biomarker currently exists for subclinical injury prior to radiological manifestation.

Voxel-wise predictive normal tissue complication probability (NTCP) models integrating dose, dose-averaged linear energy transfer (LET_d), and anatomical information generate patient-specific spatial maps of susceptibility to radiation-induced damage, extending beyond

* Corresponding author at: Department of Radiation Oncology, Heidelberg University Hospital, Im Neuenheimer Feld 451, 69120 Heidelberg, Germany.
E-mail address: habiba.sallem@med.uni-heidelberg.de (H. Sallem).

https://doi.org/10.1016/j.radonc.2026.111674
Received 14 April 2026; Received in revised form 22 June 2026; Accepted 24 June 2026
Available online 27 June 2026
0167-8140/© 2026 The Author(s). Published by Elsevier B.V. This is an open access article under the CC BY license (http://creativecommons.org/licenses/by/4.0/).

purely dosimetric region definitions by incorporating biologically heterogeneous tissue information[8–13]. Such models have demonstrated strong spatial concordance with observed CEBL locations[8] and have been applied to risk-minimizing treatment planning[9]. However, these risk maps describe population-level susceptibility at a fixed timepoint: they do not convey how tissue within at-risk regions evolves after irradiation, nor can they identify which individual patient is developing subclinical injury.

Diffusion-weighted imaging (DWI) and its derived apparent diffusion coefficient (ADC) offer a complementary, time-resolved information about tissue microstructure[14–17]. Critically, ADC signal interpretation must account for the phase of injury: in the acute post-irradiation period, vascular damage may produce cytotoxic edema with transiently restricted diffusion, while the delayed post-treatment phase — during which CEBLs typically appear — is characterized by vasogenic edema, demyelination, and tissue rarefaction, reflected as progressive ADC increases[18,19]. In this delayed phase, longitudinal ADC monitoring holds potential as an early biomarker as these increases may precede contrast enhancement by months[14–17]. Prior studies[20–22] characterizing radiation-induced diffusion changes have, however, evaluated ADC within anatomically or dosimetrically defined volumes without accounting for the spatially heterogeneous biological susceptibility captured by voxel-wise risk models.

This pilot study investigates the feasibility of risk-model-guided longitudinal ADC analysis as a post-PT surveillance framework in LGG patients. Using the Probability of Lesion Origin (POLO) model[8], a logistic-regression NTCP framework, to stratify irradiated tissue into high-risk (HR) and low-risk (LR) compartments, we examined whether temporal ADC dynamics within these regions differ between patients who subsequently develop CEBL ($CEBL^{+}$) and those who remain lesion-free ($CEBL^{-}$). We hypothesized that $CEBL^{+}$ patients would exhibit higher and more temporally variable ADC within HR regions than in LR regions — a divergence absent in $CEBL^{-}$ patients — carrying discriminative information for early identification of subclinical injury.

Materials and methods

Patient cohort and imaging acquisition

This retrospective study was approved by the Ethics Committee of Heidelberg University Hospital (ethics vote: S-056/2015).

The study included 20 patients with WHO (World Health Organization) grade II LGG (astrocytoma or oligodendroglioma), treated with actively scanned PT at the Heidelberg Ion Beam Therapy Center (*HIT, Heidelberg, Germany*). Treatment prescriptions ranged from 54–60 Gy (RBE = 1.1) delivered in 27–30 fractions. Patients were selected from the clinical cohort used by Bahn et al. [8] to develop POLO, in which DWI was acquired as part of routine follow-up but not previously analyzed. Ten patients who developed CEBLs within two years post-PT ($CEBL^{+}$) and ten who remained lesion-free ($CEBL^{-}$) were included; CEBL occurrence was defined as a binary imaging endpoint independent of toxicity grade. $CEBL^{+}$ selection was based on availability of longitudinal DWI on institutional scanners, a minimum of four pre-lesional scans, and adult age. Group-level comparability between $CEBL^{-}$ controls and $CEBL^{+}$ patients was ensured across adult age, tumor location, number of treatment fields (1-, 2-, or 3-field), and chemotherapy status, subject to the same DWI availability criteria. Patients with NTCP values significantly below the $CEBL^{+}$ range (18–35 %, median 24 %) were excluded; the $CEBL^{-}$ group had comparable modeled risk profiles (NTCP 14–28 %, median 20 %). Expansion to the full available cohort is planned.

All patients underwent quarterly MRI follow-up for up to three years, including DWI alongside T_2-weighted, FLAIR, T_1-weighted post-contrast, and perfusion sequences. $CEBL^{+}$ patients had a median follow-up of 20.8 months (range 15.0–46.9, median 6 scans, range 5–10), reflecting time to first lesion detection; only pre-lesional scans were included. $CEBL^{-}$ patients had a minimum follow-up of 10 months and a median of 25.9 months (range 9.8–37.0, median 7 scans, range 4–8), all remaining lesion-free throughout. CEBLs were identified and delineated on post-contrast T_1-weighted images as previously described [2,8]. DWI was acquired on 3 T Skyra® and Verio® scanners (*Siemens Healthineers, Germany*) using single-shot echo-planar imaging (EPI) with b-values of 0 and 1000 or 1200 s/mm^2; ADC maps were automatically generated using Siemens Syngo Via.

Polo-based regional stratification

Based on the clinical treatment plan, voxel-wise biological risk maps were generated using the Probability of Lesion Origin (POLO) model [8], a logistic-regression NTCP framework integrating physical dose, LET_d, and proximity to the ventricular system. Full model specification, including regression coefficients and computation domain, is provided in the Supplementary Material. Tissue was stratified into two compartments: a high-risk (HR) region (POLO $\geq$ 10 % of patient-specific maximum) and a low-risk (LR) region (POLO $\leq$ 1 % of maximum; Fig. 1). Thresholds were determined iteratively to yield consistent region sizes across the cohort. Voxels with intermediate POLO values (1–10 % of maximum) were deliberately excluded from both compartments to maximize biological contrast between the two comparison groups.

Image processing

ADC maps and treatment-planning CT images were processed using 3D Slicer (version 5.6.2). For each timepoint, the ADC map was rigidly co-registered to the planning CT using a mutual-information similarity metric. Although structural MRI sequences were available at each follow-up timepoint, deformable registration was attempted but yielded inconsistent results across patients, likely reflecting the limited anatomical contrast of ADC maps; rigid registration produced visually consistent alignment and was therefore retained. Registration accuracy was visually verified in three orthogonal planes, with particular attention to the alignment of the lateral, 3rd and 4th ventricles and the principal cortical sulci.

Following registration, cumulative ADC histograms were generated for the POLO-defined HR and LR regions at each time point, including the baseline scan (last MRI before start of PT). From each histogram, $ADC_{20\%}$, ADC_{mean}, and ADC_{median} ($\mu m^2/s$) were extracted. Particular emphasis was placed on $ADC_{20\%}$, defined by analogy with dose-volume histogram (DVH) metrics in radiotherapy planning as the ADC value exceeded by 20 % of voxels, corresponding to the 80th percentile of the local ADC distribution.

Longitudinal normalization and temporal quantification

Longitudinal ADC evolution was analyzed at nominal timepoints 3, 6, 9, and 12 months post-PT; scans within ±6 weeks of each timepoint were included. To remove inter-patient baseline differences, ADC metrics were expressed as percentage change relative to the individual pre-treatment baseline ($\Delta ADC_i^{baseline}$, $i = 20$ %, mean, median) for Fig. 2 and Fig. 3. Absolute ADC values were used for all statistical analyses. For each patient and region, temporal summary measures were derived from absolute ADC values: mean ADC, standard deviation (SD), coefficient of variation ($CV = \frac{SD}{mean_{ADCi}} \times 100\%$), and slope obtained from linear regression of ADC values versus actual acquisition time in months since baseline ($\mu m^2/s$ per month).

Statistical analysis

Statistical analyses were performed in Python 3.11 using SciPy and pandas. Non-parametric tests were chosen given the limited sample size.

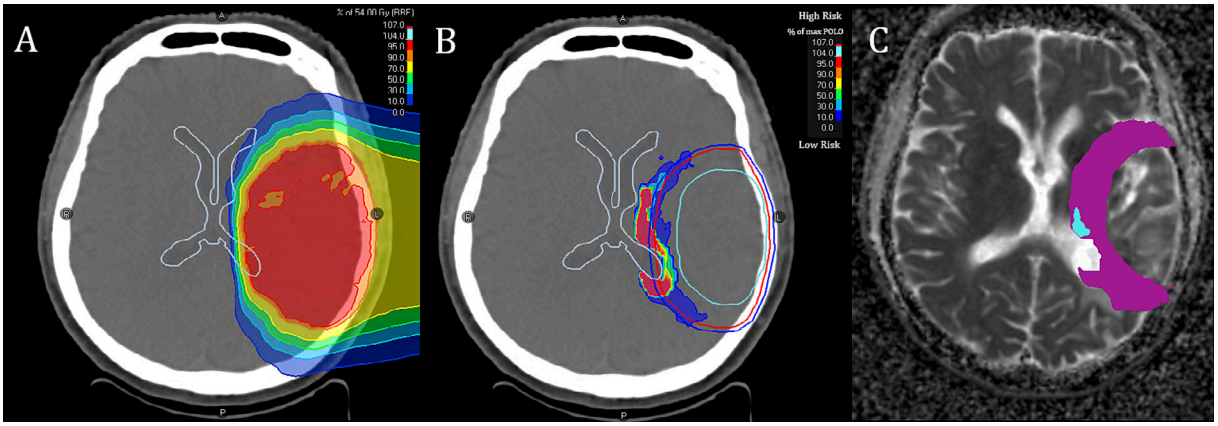


Fig. 1. POLO-based risk stratification for a representative patient (single lateral field). (A) Planning CT with RBE-weighted dose overlay (RBE = 1.1). (B) POLO risk map; warmer colors indicate higher CEBL susceptibility. (C) ADC map with POLO-defined high-risk (cyan) and low-risk (purple) overlays. (For interpretation of the references to colour in this figure legend, the reader is referred to the web version of this article.)

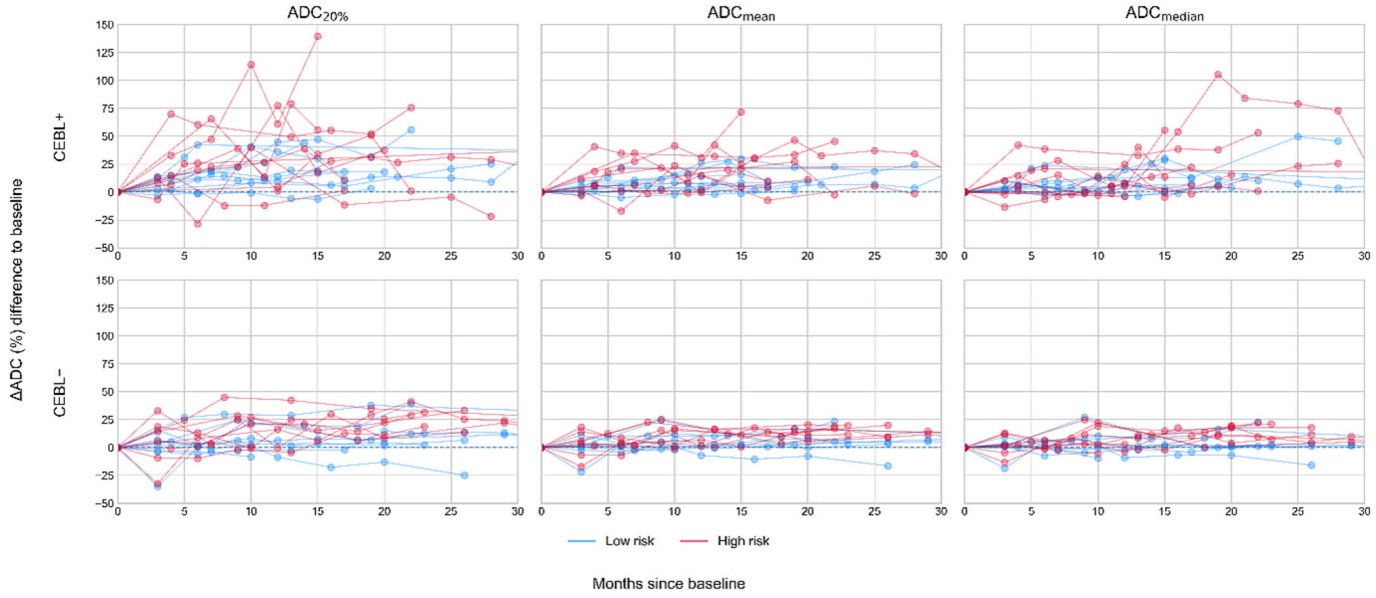


Fig. 2. Longitudinal ΔADC% relative to baseline for CEBL⁺ (top) and CEBL⁻ (bottom) groups. POLO-defined high-risk (red) and low-risk (blue) trajectories shown over months since baseline for ADC_{20}%, ADC_{mean}, and ADC_{median}. All CEBL⁺ timepoints are pre-lesional. (For interpretation of the references to colour in this figure legend, the reader is referred to the web version of this article.)

Intra-patient HR–LR comparisons used the Wilcoxon signed-rank test; inter-group comparisons (CEBL⁺ vs CEBL⁻) used the Mann–Whitney *U* test, applied to HR and LR values separately and to the per-patient HR–LR difference $\Delta(ADC_i^{HR-LR})$. Given the exploratory nature of this study, no correction for multiple comparisons was applied; p-values should be interpreted qualitatively.

Exploratory discriminative analysis

Group separation by CEBL status was evaluated at successive post-treatment timepoints using receiver operating characteristic (ROC) analysis, with performance quantified by the area under the curve (AUC). Given the limited cohort size and descriptive intent, no internal validation was performed; reported AUC values reflect group separation at individual timepoints and should not be interpreted as estimates of generalizable predictive accuracy.

Results

All longitudinal timepoints analyzed for CEBL⁺ patients were acquired before lesion onset; the last included scan per patient represents the final pre-lesional examination, with a median of 6 scans available (range 5–10). CEBL⁻ patients contributed a median of 7 scans (range 4–8).

Baseline pre-treatment ADC_i values showed no systematic differences between CEBL⁺ and CEBL⁻ patients or between HR and LR regions within either group, indicating comparable starting conditions.

Fig. 2 shows the longitudinal ΔADC% trajectories for all patients in both groups. Individual patient trajectories with rescaled axes to highlight inter-patient variability are shown in Supplementary Fig. S1. In CEBL⁺ patients (top panels), HR tissue showed a progressive group-level increase in $ADC_{20\%}$ and ADC_{mean} across the follow-up period, while individual trajectories exhibited variability; ADC_{median} showed the same directional trend with greater inter-patient variability. In CEBL⁻ patients (bottom panels), both regions exhibited minimal temporal change, with HR and LR trajectories remaining closely aligned.

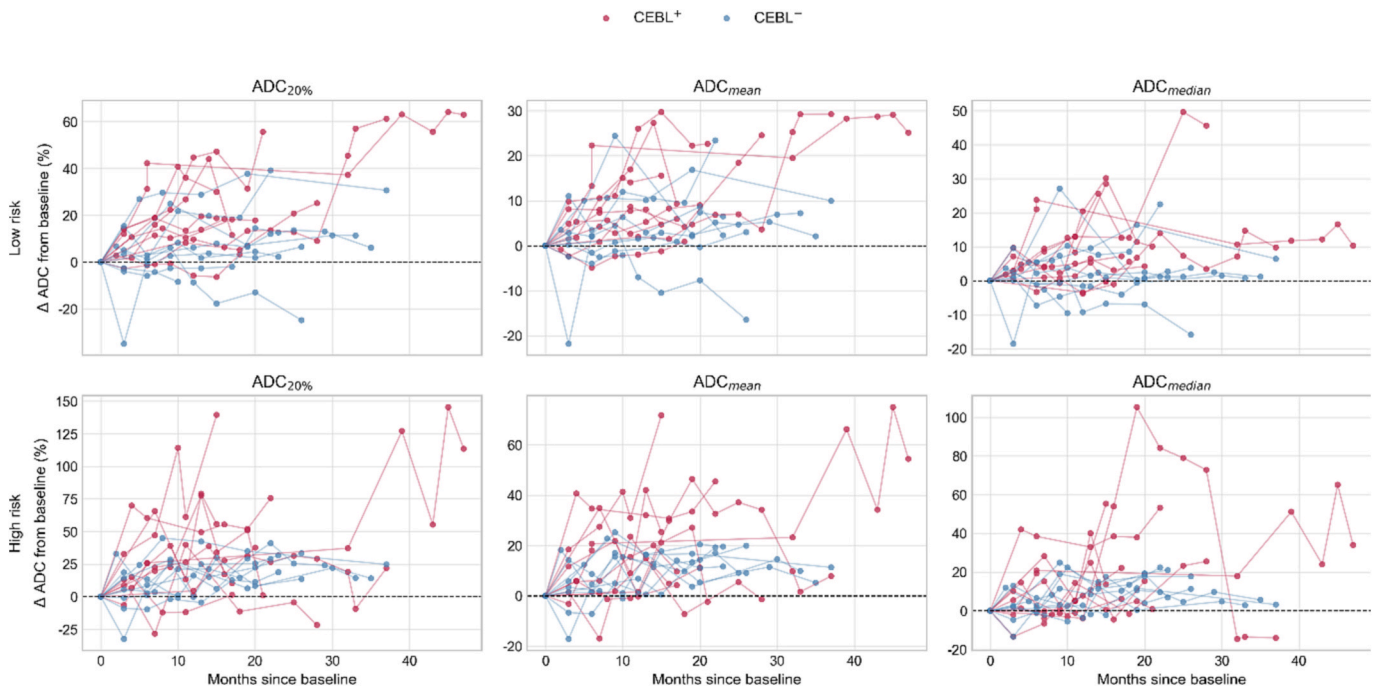


Fig. 3. ΔADC_i over time for all patients by POLO-defined risk region (HR, LR) and CEBL status (CEBL⁺: red, CEBL⁻: blue). (For interpretation of the references to colour in this figure legend, the reader is referred to the web version of this article.)

Across the cohort (Fig. 3), HR regions in CEBL⁺ patients consistently showed higher diffusion values and greater temporal variability than LR regions. For $ADC_{20\%}$, CEBL⁺ HR tissue averaged 1699 ± 333 $\mu m^2/s$, significantly higher than LR tissue (1373 ± 170 $\mu m^2/s$, $p = 0.02$). No HR–LR difference was observed in CEBL⁻ patients (1344 ± 249 $\mu m^2/s$ vs 1359 ± 196 $\mu m^2/s$, $p = 0.91$). ADC_{mean} followed the same pattern: HR regions were elevated in CEBL⁺ (1224 ± 146 $\mu m^2/s$) relative to LR (1085 ± 83 $\mu m^2/s$, p = 0.01), with no difference in CEBL⁻ ($p = 0.91$). ADC_{median} showed the same directional trend in CEBL⁺ (HR: 1408 ± 187 vs LR: 1203 ± 98 $\mu m^2/s$, $p = 0.13$) without reaching significance, and no difference in CEBL⁻ ($p = 0.25$).

Intra-regional temporal heterogeneity, expressed as coefficient of variation (CV), was markedly greater in CEBL⁺ HR regions (18.9 ± 7.4 %) than LR regions (10.2 ± 4.6 %). In CEBL⁻ patients, CV values were lower and comparable between HR (10.0 ± 3.6 %) and LR (7.2 ± 3.9 %) regions. Temporal slopes followed the same pattern: HR regions in CEBL⁺ patients increased by 20.9 ± 26.7 $\mu m^2/s$ per month versus 14.1 ± 8.0 $\mu m^2/s$ per month in LR; CEBL⁻ patients showed modest slopes in both regions (HR: 8.9 ± 6.2; LR: 2.6 ± 8.6 $\mu m^2/s$/month). All quantitative descriptors are summarized in Table 1.

CEBL⁺ patients showed a significantly larger $\Delta(ADC_{20\%}^{HR-LR})$ than CEBL⁻ patients across the follow-up period (p = 0.02, Fig. 4), with the divergence increasing over the first post-treatment year. $\Delta(ADC_{mean}^{HR-LR})$ and $\Delta(ADC_{median}^{HR-LR})$ showed directionally consistent but non-significant differences (p = 0.07 and p = 0.21, respectively). Exploratory logistic regression using $\Delta(ADC_{20}$%HR-LR) as the sole predictor yielded AUC values of 0.70–0.79 across the four quarterly timepoints, with the strongest group separation at the six-month timepoint (AUC = 0.79).

Discussion

This pilot feasibility study combined voxel-wise predictive risk

Table 1
Longitudinal ADC summary metrics by risk region and CEBL status. Values are mean ± SD; $ADC_{20\%}$, ADC_{mean}, and ADC_{median} in $\mu m^2/s$. p_1: HR vs LR (Wilcoxon signed-rank); p_2: CEBL⁺ vs CEBL⁻ within region (Mann-Whitney U); p_3: HR–LR difference between groups (Mann-Whitney U).

Group	Region	Mean ± SD [$\mu m^2/s$]	CV (%) ± SD	Slope ± SD [$\mu m^2/s$/month]	p_1 (HR vs LR)	p_2 (CEBL⁺ vs CEBL⁻)	p_3 ($\Delta(ADC_i^{HR-LR})$)
ADC_{20} %					0.02	0.91	0.02
CEBL⁺	HR	1699 ± 333	18.9 ± 7.4	20.9 ± 26.7			
	LR	1373 ± 170	10.2 ± 4.6	14.1 ± 8.0			
CEBL⁻	HR	1344 ± 249	10.0 ± 3.6	8.9 ± 6.2			
	LR	1359 ± 196	7.2 ± 3.9	2.6 ± 8.6			
ADC_{mean}					0.01	0.91	0.07
CEBL⁺	HR	1224 ± 146	17.3 ± 5.9	18.6 ± 21.2			
	LR	1085 ± 83	9.4 ± 3.2	10.8 ± 6.6			
CEBL⁻	HR	1097 ± 157	8.9 ± 3.1	6.8 ± 5.4			
	LR	1109 ± 142	6.5 ± 2.7	3.1 ± 7.1			
ADC_{median}					0.13	0.25	0.21
CEBL⁺	HR	1408 ± 187	15.8 ± 6.4	17.2 ± 17.9			
	LR	1203 ± 98	8.7 ± 3.7	9.6 ± 7.5			
CEBL⁻	HR	1229 ± 171	9.1 ± 3.2	7.1 ± 5.6			
	LR	1242 ± 158	6.8 ± 2.9	3.5 ± 6.9			

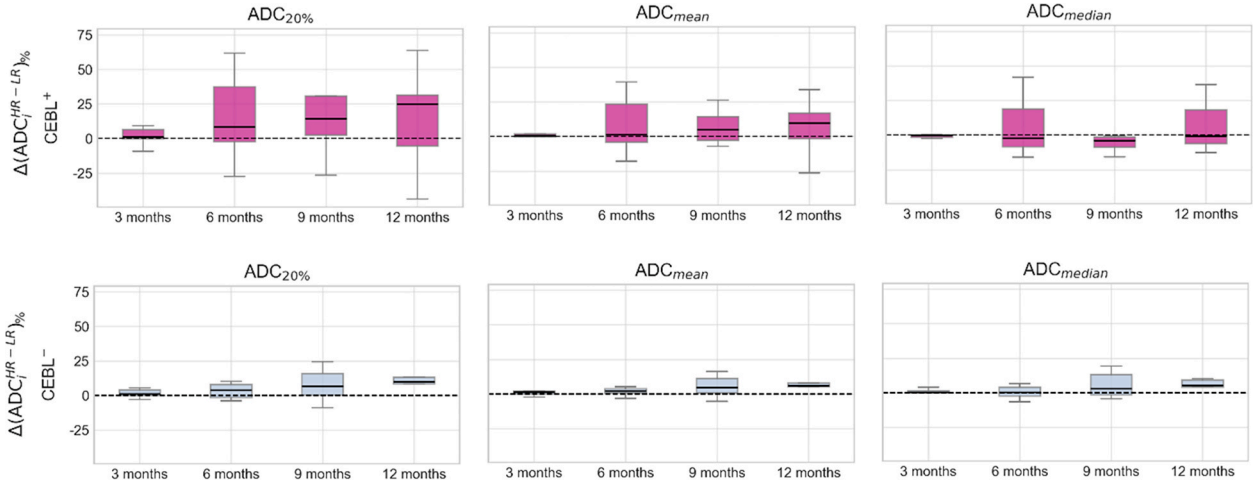


Fig. 4. $\Delta(ADC_i^{HR\text{-}LR})$ boxplots across four quarterly timepoints for $ADC_{20\%}$, ADC_{mean}, ADC_{median}, by CEBL status.

modeling with longitudinal diffusion MRI to characterize early post-PT tissue dynamics in LGG patients. By stratifying the irradiated brain into risk-model-defined compartments and tracking respective ADC trajectories, the analysis revealed systematically distinct behavior between CEBL⁺ and CEBL⁻ patients. The intra-patient HR–LR $ADC_{20\%}$ difference ($\Delta(ADC_{20\%}^{HR\text{-}LR})$) provided the strongest group separation, with an exploratory AUC of 0.79 at six months post-treatment — approximately 12 months before CEBL detection (mean 18 months post-PT[2]). The observed ADC elevations in HR tissue of CEBL⁺ patients are consistent with delayed post-radiation changes: ADC increases have been associated with cell loss, demyelination, and microvascular damage preceding macroscopic contrast enhancement [17,18,23].

Most prior imaging work has characterized these changes at the level of established lesions — distinguishing radiation necrosis from tumor recurrence using ADC, diffusion tensor imaging (DTI), or metabolic signatures [14,23,24] — or evaluated diffusion metrics averaged across entire irradiated volumes [25,26]. These approaches inherently conflate tissue with heterogeneous biological susceptibility. The pre-lesional trajectory analyzed here precedes morphological and contrast changes [7] when spatially localized microstructural alterations may already be evolving.

The central methodological contribution is the use of a spatially explicit risk model to define tissue compartments for longitudinal diffusion analysis. Rather than anatomical or dosimetric regions, we applied the POLO model [8] to isolate subvolumes of spatially heterogeneous radiobiological susceptibility — reflecting location-dependent LET_d and periventricular radiosensitivity — distinct from dynamic tissue-level biological heterogeneity not captured by the current static model. Computing the intra-patient HR–LR ADC contrast suppresses between-patient variability in baseline diffusivity and normalizes for differences in scanner, protocol, and tumor location — a rationale similarly applied in temporal ADC monitoring of glioblastoma[22]. Preliminary analysis within dosimetrically defined regions yielded no discriminative signal between groups, directly motivating the POLO-based approach.

Among evaluated diffusion map metrics, $ADC_{20\%}$ provided the most consistent discrimination. By analogy with DVH conventions, $ADC_{20\%}$ reflects the value exceeded by the most diffusion-elevated 20 % of voxels, capturing localized early microstructural disorganization while remaining less sensitive to global distribution shifts [14,16].

The appearance of discriminative diffusion signal within risk-model-defined HR regions at six months post-PT supports a potential role for this framework in post-treatment imaging surveillance. CEBLs are associated with neurological morbidity [27], and share vascular risk factor profiles with ischemic cerebrovascular events, suggesting subpopulations for whom early identification may be particularly consequential [28].

The patient-level NTCP derived from the POLO model characterizes pre-treatment risk based on dosimetric and anatomical parameters, but contains no information about the tissue's biological response after irradiation. Longitudinal ADC monitoring within POLO-defined regions adds a time-resolved, patient-specific biological dimension that is complementary to, rather than competing with, pre-treatment risk stratification. The required inputs — DWI sequences, LET_d distributions, ventricular contours, and physical dose — are increasingly available within standard clinical workflows. Integration of the registration and ADC extraction pipeline into treatment planning systems or picture archiving and communication systems environments would enable risk-adapted surveillance, directing radiological attention to HR tissue and informing follow-up scheduling based on observed ADC trajectories.

Several limitations should be considered. The cohort was restricted to 20 patients from a single institution; patients were drawn from the same dataset used to develop the POLO model [8], and prospective external validation is essential. ADC maps were rigidly co-registered to the planning CT without EPI distortion correction; deformable registration was attempted but yielded inconsistent results and was not retained — prospective implementation will incorporate deformable registration with structural MRI alignment. Residual misregistration effects are partially mitigated by the spatial co-localization of HR and LR regions, such that systematic distortions partially cancel in the HR–LR difference metric. DWI was acquired on two scanner models with minor b-value variation; baseline normalization partially mitigates this variability. The cohort includes patients treated with one-, two- and three-field arrangements [29]; the relationship between field number and ADC trajectories warrants future investigation.

Conclusions

The combination of longitudinal diffusion MRI with voxel-level risk-modelling provided quantitative insight into early tissue responses after PT for LGG. Patients who developed CEBLs showed greater temporal variability and steeper diffusion increases within HR regions, whereas CEBL⁻ patients remained stable. ADC_{20}% within HR tissue most effectively distinguished these trajectories; the intra-patient HR–LR difference $\Delta(ADC_{20\%}^{HR\text{-}LR})$ yielded exploratory AUCs of 0.70–0.79 across post-treatment timepoints in this pilot cohort. These findings support risk-adapted ADC monitoring for early detection of subclinical tissue changes after PT.

Fundings

HS: "Alois Hirdt-Erben und Wieland" Foundation. JB: "Alois Hirdt-Erben und Wieland" foundation, Olympia-Morata Program (Heidelberg University). SH: German Research Foundation (DFG). Ethics committee of the medical faculty of Heidelberg university S-516/2022.

CRediT authorship contribution statement

Habiba Sallem: Writing – review & editing, Writing – original draft, Visualization, Methodology, Investigation, Formal analysis, Data curation, Conceptualization. **Semi Harrabi:** Supervision, Methodology, Investigation, Formal analysis. **Michael O. Breckwoldt:** Writing – review & editing, Writing – original draft, Supervision, Methodology, Investigation, Formal analysis, Conceptualization. **Klaus Herfarth:** Supervision, Investigation, Conceptualization. **Jürgen Debus:** Resources, Funding acquisition. **Julia Bauer:** Writing – review & editing, Writing – original draft, Validation, Supervision, Investigation, Data curation, Conceptualization.

Declaration of competing interest

The authors declare that they have no known competing financial interests or personal relationships that could have appeared to influence the work reported in this paper.

Appendix A. Supplementary data

Supplementary data to this article can be found online at https://doi.org/10.1016/j.radonc.2026.111674.

References

[1] Underwood TSA, McNamara AL, Appelt A, Haviland JS, Sørensen BS, Troost EGC. A systematic review of clinical studies on variable proton Relative Biological Effectiveness (RBE). Radiother Oncol 2022;175:79–92. https://doi.org/10.1016/j.radonc.2022.08.014.

[2] Harrabi SB, von Nettelbladt B, Gudden C, et al. Radiation induced contrast enhancement after proton beam therapy in patients with low grade glioma – How safe are protons? Radiother Oncol 2022;167:211–8. https://doi.org/10.1016/j.radonc.2021.12.035.

[3] Merchant TE, Conklin HM, Wu S, Lustig RH, Xiong X. Late Effects of Conformal Radiation Therapy for Pediatric Patients With Low-Grade Glioma: Prospective Evaluation of Cognitive, Endocrine, and Hearing Deficits. *Journal of Clinical Oncology*. Published online August 1, 2009. doi:10.1200/JCO.2008.21.2738.

[4] Wilke C, Grosshans D, Duman J, Brown P, Li J. Radiation-induced cognitive toxicity: pathophysiology and interventions to reduce toxicity in adults. Neuro Oncol 2018;20(5):597–607. https://doi.org/10.1093/neuonc/nox195.

[5] Kumar AJ, Leeds NE, Fuller GN, et al. Malignant gliomas: MR imaging spectrum of radiation therapy- and chemotherapy-induced necrosis of the brain after treatment. Radiology 2000;217(2):377–84. https://doi.org/10.1148/radiology.217.2.r00nv36377.

[6] Karschnia P, Nelson TA, Dietrich J. Mechanisms and treatment of cancer therapy-induced peripheral and central neurotoxicity. Nat Rev Cancer 2025:1–23. https://doi.org/10.1038/s41568-025-00863-2.

[7] Wang S, Tryggestad E, Zhou T, et al. Assessment of MRI parameters as imaging biomarkers for radiation necrosis in the rat brain. Int J Radiat Oncol Biol Phys 2012;83(3):e431–6. https://doi.org/10.1016/j.ijrobp.2011.12.087.

[8] Bahn E, Bauer J, Harrabi S, Herfarth K, Debus J, Alber M. Late contrast enhancing brain lesions in proton-treated patients with low-grade glioma: clinical evidence for increased periventricular sensitivity and variable RBE. International Journal of Radiation Oncology*Biology*Physics. 2020;107(3):571–8. https://doi.org/10.1016/j.ijrobp.2020.03.013.

[9] Sallem H, Harrabi S, Traneus E, Herfarth K, Debus J, Bauer J. A model-based risk-minimizing proton treatment planning concept for brain injury prevention in low-grade glioma patients. Radiother Oncol 2024;201:110579. https://doi.org/10.1016/j.radonc.2024.110579.

[10] Eulitz J, Troost EGC, Raschke F, et al. Predicting late magnetic resonance image changes in glioma patients after proton therapy. Acta Oncol 2019;58(10):1536–9. https://doi.org/10.1080/0284186X.2019.1631477.

[11] Eulitz J, Troost E GC, Klünder L, et al. Increased relative biological effectiveness and periventricular radiosensitivity in proton therapy of glioma patients. Radiother Oncol 2023;178:109422. https://doi.org/10.1016/j.radonc.2022.11.011.

[12] Palkowitsch M, Kaufmann LM, Hennings F, et al. Variable-RBE-induced NTCP predictions for various side-effects following proton therapy for brain tumors – Identification of high-risk patients and risk mitigation. Radiother Oncol 2025;202:110590. https://doi.org/10.1016/j.radonc.2024.110590.

[13] Palkowitsch M, Kilian LS, Hennings F, et al. Model validation confirms variable relative biological effectiveness and elevated periventricular sensitivity after proton therapy of brain tumors. Radiother Oncol 2026;214:111271. https://doi.org/10.1016/j.radonc.2025.111271.

[14] Asao C, Korogi Y, Kitajima M, et al. Diffusion-Weighted Imaging of Radiation-Induced Brain Injury for Differentiation from Tumor Recurrence. AJNR Am J Neuroradiol 2005;26(6):1455–60.

[15] Mullins ME, Barest GD, Schaefer PW, Hochberg FH, Gonzalez RG, Lev MH. Radiation necrosis versus glioma recurrence: conventional MR imaging clues to diagnosis. AJNR Am J Neuroradiol 2005;26(8):1967–72.

[16] Le Bihan D, Iima M. Diffusion Magnetic Resonance Imaging: What Water Tells Us about Biological Tissues. PLoS Biol 2015;13(7):e1002203. https://doi.org/10.1371/journal.pbio.1002203.

[17] Sugahara T, Korogi Y, Kochi M, et al. Usefulness of diffusion-weighted MRI with echo-planar technique in the evaluation of cellularity in gliomas. J Magn Reson Imaging 1999;9(1):53–60. https://doi.org/10.1002/(sici)1522-2586(199901)9:1<53::aid-jmri7>3.0.co;2-2.

[18] Walker AJ, Ruzevick J, Malayeri AA, et al. Postradiation imaging changes in the CNS: how can we differentiate between treatment effect and disease progression? Future Oncol 2014;10(7):1277–97. https://doi.org/10.2217/fon.13.271.

[19] Katsura M, Sato J, Akahane M, Furuta T, Mori H, Abe O. Recognizing Radiation-induced Changes in the Central Nervous System: Where to Look and What to Look For. Radiographics 2021;41(1):224–48. https://doi.org/10.1148/rg.2021200064.

[20] Hope TR, Vardal J, Bjørnerud A, et al. Serial diffusion tensor imaging for early detection of radiation-induced injuries to normal-appearing white matter in high-grade glioma patients. J Magn Reson Imaging 2015;41(2):414–23. https://doi.org/10.1002/jmri.24533.

[21] Raschke F, Wesemann T, Wahl H, et al. Reduced diffusion in normal appearing white matter of glioma patients following radio(chemo)therapy. Radiother Oncol 2019;140:110–5. https://doi.org/10.1016/j.radonc.2019.06.022.

[22] Moore-Palhares D, Lawrence LSP, Myrehaug S, et al. Temporal Apparent Diffusion Coefficient Changes During Chemoradiation: An Imaging Biomarker for Tumor Response Monitoring and Spatial Recurrence Prediction in Glioblastoma. Int J Radiat Oncol Biol Phys 2025;122(3):592–604. https://doi.org/10.1016/j.ijrobp.2025.03.028.

[23] Sundgren PC, Fan X, Weybright P, et al. Differentiation of recurrent brain tumor versus radiation injury using diffusion tensor imaging in patients with new contrast-enhancing lesions. Magn Reson Imaging 2006;24(9):1131–42. https://doi.org/10.1016/j.mri.2006.07.008.

[24] Zhou J, Tryggestad E, Wen Z, et al. Differentiation between glioma and radiation necrosis using molecular magnetic resonance imaging of endogenous proteins and peptides. Nat Med 2011;17(1):130–4. https://doi.org/10.1038/nm.2268.

[25] Bušić M, Rumboldt Z, Čerina D, Bušić Ž, Dolić K. Prognostic Value of Apparent Diffusion Coefficient (ADC) in Patients with Diffuse Gliomas. Cancers (Basel) 2024;16(4):681. https://doi.org/10.3390/cancers16040681.

[26] Verma N, Cowperthwaite MC, Burnett MG, Markey MK. Differentiating tumor recurrence from treatment necrosis: a review of neuro-oncologic imaging strategies. Neuro Oncol 2013;15(5):515–34. https://doi.org/10.1093/neuonc/nos307.

[27] Lütgendorf-Caucig C, Pelak M, Hug E, et al. Prospective analysis of radiation-induced contrast enhancement and health-related quality of life after proton therapy for central nervous system and skull base tumors. Int J Radiat Oncol Biol Phys 2024;118(5):1206–16. https://doi.org/10.1016/j.ijrobp.2024.01.007.

[28] Eichkorn T, Lischalk JW, Schwarz R, et al. Radiation-induced cerebral contrast enhancements strongly share ischemic stroke risk factors. Int J Radiat Oncol Biol Phys 2024;118(5):1192–205. https://doi.org/10.1016/j.ijrobp.2023.12.044.

[29] Bauer J, Bahn E, Harrabi S, Herfarth K, Debus J, Alber M. How can scanned proton beam treatment planning for low-grade glioma cope with increased distal RBE and locally increased radiosensitivity for late MR-detected brain lesions? Med Phys 2021;48(4):1497–507. https://doi.org/10.1002/mp.14739.